

High-throughput Li plating quantification for fast charging battery design

Zachary Konz

Department of Chemical and Biomolecular Engineering, University of California, Berkeley, Berkeley, CA, USA <https://orcid.org/0000-0002-0346-7605>

Brendan Wirtz

Department of Chemical and Biomolecular Engineering, University of California, Berkeley, Berkeley, CA, USA <https://orcid.org/0000-0002-7489-4399>

Ankit Verma

Transportation and Hydrogen Systems Center, National Renewable Energy Laboratory, Golden, CO, USA <https://orcid.org/0000-0002-7610-8574>

Tzu-Yang Huang

Department of Chemical and Biomolecular Engineering, University of California, Berkeley, Berkeley, CA, USA

Helen Bergstrom

Department of Chemical and Biomolecular Engineering, University of California, Berkeley, Berkeley, CA, USA

Matthew Crafton

Department of Chemical and Biomolecular Engineering, University of California, Berkeley, Berkeley, CA, USA <https://orcid.org/0000-0001-7228-5576>

David Brown

Department of Chemical and Biomolecular Engineering, University of California, Berkeley, Berkeley, CA, USA

Eric McShane

Department of Chemical and Biomolecular Engineering, University of California, Berkeley, Berkeley, CA, USA

Andrew Colclasure

Transportation and Hydrogen Systems Center, National Renewable Energy Laboratory, Golden, CO, USA <https://orcid.org/0000-0002-9574-5106>

Bryan McCloskey (✉ bmcclosk@berkeley.edu)

Department of Chemical and Biomolecular Engineering, University of California, Berkeley, Berkeley, CA, USA <https://orcid.org/0000-0001-6599-2336>

Keywords:

Posted Date: July 1st, 2022

DOI: <https://doi.org/10.21203/rs.3.rs-1805434/v1>

License:   This work is licensed under a Creative Commons Attribution 4.0 International License.

[Read Full License](#)

High-throughput Li plating quantification for fast charging battery design

Zachary M. Konz^{1,2}, Brendan M. Wirtz^{1*}, Ankit Verma³, Tzu-Yang Huang^{1,2}, Helen K. Bergstrom^{1,2}, Matthew J. Crafton^{1,2}, David E. Brown^{1,2}, Eric J. McShane^{1,2*}, Andrew M. Colclasure³, Bryan D. McCloskey^{1,2}

1. Department of Chemical and Biomolecular Engineering, University of California, Berkeley, Berkeley, CA, USA
 2. Energy Storage and Distributed Resources Division, Lawrence Berkeley National Laboratory, Berkeley, CA, USA
 3. Transportation and Hydrogen Systems Center, National Renewable Energy Laboratory, Golden, CO, USA
- * Present address: Department of Chemical Engineering, Stanford University, Stanford, CA, USA

Abstract

Fast charging of most commercial lithium-ion batteries is limited due to fear of lithium plating on the graphite anode, which is difficult to detect and poses significant safety risk. Here we demonstrate the power of simple, accessible, and high-throughput cycling techniques to quantify irreversible Li plating spanning data from over 200 cells. We first observe the effects of energy density, charge rate, temperature, and State-of-Charge (SOC) on lithium plating, use the results to refine mature physics-based electrochemical models, and provide an interpretable empirical equation for predicting the plating onset SOC. We then explore the reversibility of lithium plating for varied deposition rates, amounts, and electrolyte compositions, applying our understanding towards development of electrolytes that reduce irreversible Li formation. Finally, we provide the first quantitative comparison of lithium plating in the experimentally convenient Graphite|Li cell configuration compared with commercially relevant Graphite|LiNi_{0.5}Mn_{0.3}Co_{0.2}O₂ (NMC). The hypotheses and abundant data herein were generated primarily with equipment universal to the battery researcher, encouraging further development of innovative testing methods and data processing that enable rapid battery engineering.

Introduction

The urgent need to combat climate change has sparked extreme growth in demand for lithium-ion batteries (LIB). Rapid innovation in battery materials and cell design is critical to meet this demand for diverse applications from electronics to vehicles and utility-scale energy storage. Composite graphite electrodes remain a universal component of the LIB and are expected to dominate anode market share through 2030 despite the introduction of silicon and lithium-based materials¹.

The design space for graphite electrodes is immense, with parameters such as the loading, porosity, particle size, binder composition, and electrolyte being carefully selected to meet requirements for lifetime, operating temperature, charge time, and manufacturing. Regardless of design and application, the lithium plating reaction on graphite is a performance and safety concern due to the formation of non-cyclable ‘dead’ lithium metal and salts. While recent studies have focused on Li plating during fast charging, the phenomenon is also pertinent to other operating extremes such as low temperature², overcharge³, or system malfunction⁴.

Electrochemical (EChem) modeling is an important tool for understanding design tradeoffs that improve graphite performance while avoiding plating. Over decades, Newman-based models that relate cell current density, voltage, temperature, and material properties to graphite intercalation have been enhanced to also estimate lithium plating.^{5–10} This has led to initial insight into the effect of charge rate, electrode loading, and temperature on lithium plating onset/amount, but simulations rely on debated parameters such as the plating exchange current density or reversibility and are frequently not verified with direct experimental measurements¹¹ such as Li gas evolution titrations^{12,13}. EChem models also have limited ability to predict the chemical compatibility and interphasial properties for novel electrolytes. High-throughput modeling advances for battery materials and interfaces could fill this void, but they too lack commensurate validation¹⁴.

Challenges to high-throughput battery testing can include limited access to expensive equipment, slow multiweek cycling tests, limited material availability, high labor cost of cell assembly, complex analysis methods, and inefficient data handling. There are promising solutions to some of these problems. To conserve newly synthesized electrode materials, it is common practice to determine charge rate capabilities by testing multiple rates on a single cell^{15,16}. High-precision coulometers have been developed to improve early performance prediction^{17,18}. Data-driven models that predict cycle life from minimal data¹⁹ can be used to quickly optimize charge protocols²⁰, although large data sets are difficult to obtain in most laboratory settings²¹.

Here we demonstrate the power of simple, quantitative, and accessible cycling protocols to inform battery design for Li plating-free charging. The tradeoffs between energy density, charge rate, charge temperature, and lithium plating are experimentally quantified and used to refine mature electrochemical models. We then explore the reversibility of lithium plating under varied fast charging conditions, and apply our understanding towards development of electrolytes and interfaces that limit dead Li formation. We emphasize that the hypotheses and abundant data presented herein were generated primarily with equipment universal to the battery researcher, enabled by strategic data handling, while the sophisticated modeling and titration techniques were reserved for secondary support of the findings.

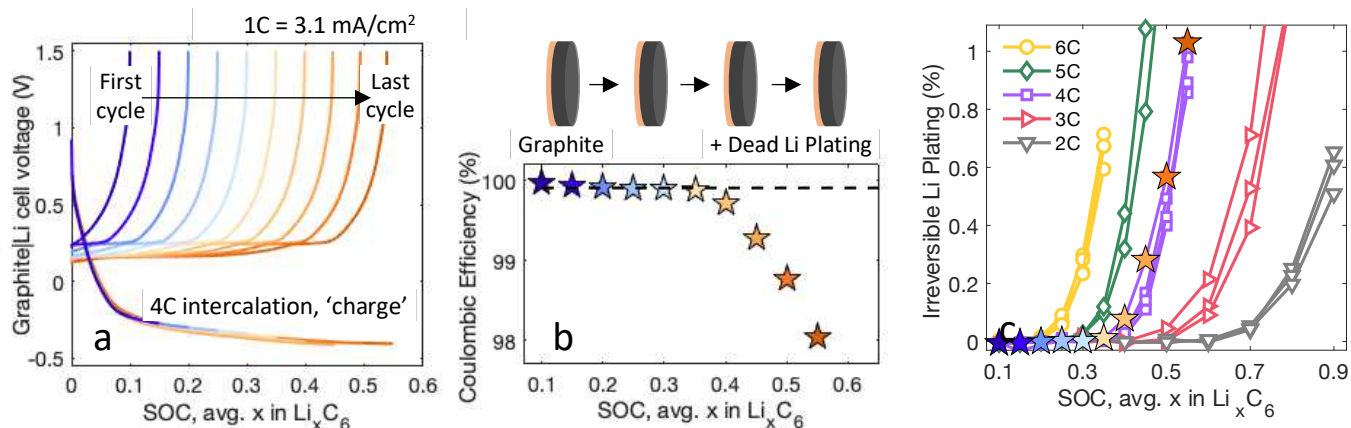


Fig. 1 | Determining irreversible Li plating as a function of charge rate and length. **a**, SOC-sweep cycling protocol to test charging performance at 4C to varied states-of-charge. **b**, CEs from the cycling in (a) show a drop around 40% SOC, indicating the accumulation of irreversible Li plating. **c**, The CEs are recast as an irreversible lithium capacity by subtracting all CEs from the high-CE plateau (dashed line in **b**) and multiplying the resulting CIE% by the normalized charge capacity. Additional data are overlaid for this condition (3.1 mAh/cm², 25°C) with charge rates of 6C (n=4), 5C (n=2), 4C (n=4), 3C (n=3), and 2C (n=3). For this electrode, 1% is ~31 $\mu\text{Ah}/\text{cm}^2$ and varies slightly with cell capacity ($3.11 \pm 0.05 \text{ mAh}/\text{cm}^2$).

Irreversible Li mapping and modeling

Past independent titration studies of Li plating on copper¹² and graphite¹³ both show a strong positive correlation between coulombic inefficiency and inactive Li^0 , with the majority of the irreversible plating capacity attributed to H_2 -evolving dead Li species (Li^0 , Li_xC_6) for liquid carbonate-based electrolytes. This observation combined with the high-throughput, precise nature of Graphite|Li cell coulombic efficiency (CE) measurements motivated the protocol in Figure 1 to estimate irreversible Li plating as a function of charge length. We define irreversible Li as the sum of irreversibly formed species during Li plating such as isolated metallic lithium and Li^+ -containing solid-electrolyte interphase (SEI). After formation cycling (see Methods), the 4C charge capacity is increased stepwise by 5% State-of-Charge (SOC), or normalized graphite capacity, for each cycle from 10% to 55% SOC (Fig. 1a). Here we refer to graphite intercalation as ‘charge’ despite the decreasing cell voltage in the Gr|Li half-cell configuration. We previously demonstrated this ‘SOC-sweep’ approach to study plating with differential voltage analysis²², and a similar stepwise capacity cycling has been used for Gr|Cathode full-cells²³, but here we first focus on half-cells due to the stable potential of the Li counter electrode and desire to isolate graphite anode degradation effects.

The CE for each of the cycles is shown vs charge capacity in Figure 1b. To estimate the irreversible Li, a high-efficiency baseline CE (dashed line) is first assigned to the data points at low SOC, where we attribute the non-unity values to continued SEI formation or slow cell degradation processes rather than Li plating. CE data are then subtracted from these baselines, ranging 99.85-99.98% (see Fig. S1), to yield a coulombic inefficiency (CIE) from Li plating-related degradation. The CIE multiplied by the SOC for each cycle gives irreversible plating capacities as a percent of each cell’s experimental capacity, which are shown in Fig. 1c for various rates, with the result of each cell represented by a set of connected data points. Throughout this work, we point out ways that cycling data, modeling, and titrations further confirm the reliability of CIE for irreversible Li plating quantification. To start, Fig. 1c data reproducibly shows the expected trend of earlier SOC onsets for Li plating as the rate of fast charging is increased from 2C to 6C. Supplementary Information Figs. S2-S3 discuss protocol development, SOC range selection, and control experiments that show minimal cell aging effects for the SOC-sweep method, whereas Fig. S4 supports the link between CIE and irreversible plating.

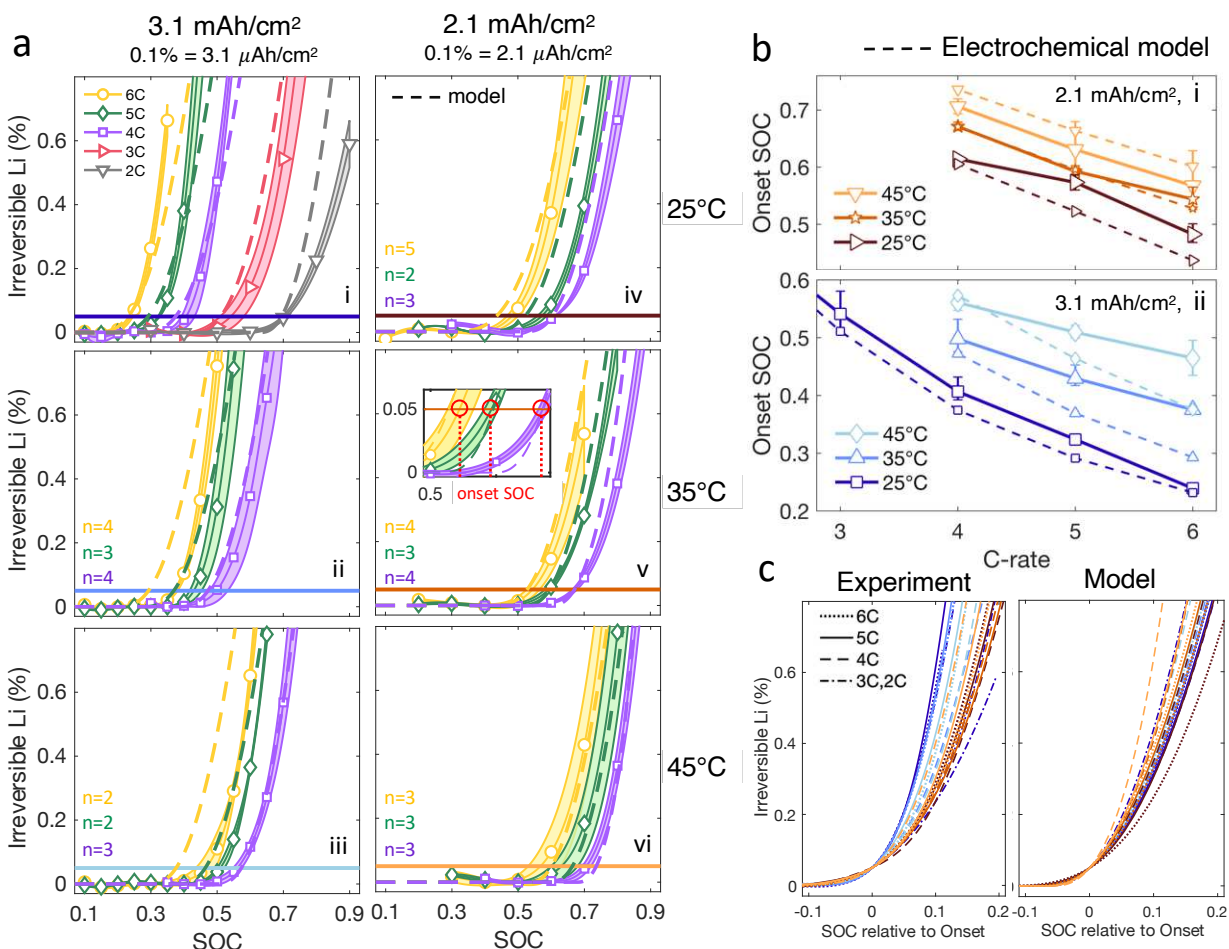


Fig. 2 | Irreversible Li plating and plating onsets with modeling. **a**, Irreversible lithium averages and standard deviations for rates 2C–6C for graphite loadings of 3.1 mAh/cm² (left) and 2.1 mAh/cm² (right) at 25°C (top), 35°C (middle), and 45°C (bottom). Data are interpolated with a cubic spline and number of cells n are listed for each condition (see Fig. S3.3). Electrochemical model simulations are in dashed lines and assume 70% plating reversibility. **b**, Lithium plating onsets are the SOC where irreversible Li exceeds 0.05% or 1.0–1.5 $\mu\text{Ah}/\text{cm}^2$, shown in the a–v inset. Model results are in dashed lines. **c**, Experimental (left) and modeled (right) irreversible Li plating curves shifted in the x-direction by their respective plating onset SOC. The colors correspond to the unique [temperature, loading] combinations as in b, and the rate is depicted by the line style.

Increasing the charge temperature is a well-known operating control to avoid lithium plating but, to the best of our knowledge, no work has simultaneously quantified the effects across charge rates (C-rates), loadings, and SOC, all relevant for battery design. Figure 2a shows the irreversible Li plating estimated from the high-throughput SOC-sweep for graphite loadings of 3.1 mAh/cm² (left) and 2.1 mAh/cm² (right) at 25°C (top), 35°C (middle), and 45°C (bottom). The data points are experimental averages and the shaded regions are constructed from the standard deviations calculated at each SOC; the averaging process is illustrated by comparing Fig. 1c and Fig. 2a–i. The technique fidelity is supported by experimental trends that are universally consistent with the expectation that the starting SOC of lithium plating should be postponed with decreasing current rates (left to right within panels), decreasing loadings (left to right across panels), and increasing temperature (top to bottom), as seen in shifting irreversible Li curves in the x-direction.

Irreversible Li estimates from a previously reported Newman EChem model^{9,24–26} are overlaid with experiment in Figure 2a. The lithium plating reaction is modeled using the formulation proposed by Ren et al.⁸, with a plating exchange current density of 10 A/m² and fixed plating reversibility of 70%, both

estimated under fast charge conditions with modest amounts of plating (~1% of graphite capacity) using gas evolution titrations and voltage profiles¹³. Specific parameters for these electrodes and electrolyte transport properties have been extensively reported and are in Table S3 along with experimental and modeled voltage profiles in Figs. S5 and S6. The excellent qualitative agreement in irreversible Li curve shape between model and experiment increases confidence in both the exponential Butler-Volmer kinetic expression used for lithium plating/stripping as well as the assumption that experimental capacity loss is mostly due to irreversible Li instead of other slower degradation processes.

From this dataset we extract the SOC at which irreversible Li starts to form, or ‘plating onset’, as a metric to inform safe charge durations and assess the quality of our experiment-model agreement. Here we define the plating onset threshold as 0.05% irreversible Li, or 1.0-1.5 $\mu\text{Ah}/\text{cm}^2$ for the respective electrode loadings, which is represented by the horizontal lines in Fig. 2a. This is the lowest value after which clear plating increases are observed and also avoids uncertainty from experimental noise at low SOC (Fig. 2a-iv, bottom left). The SOC at which plating begins for all 20 conditions are shown in Figure 2b. Reasonably linear relationships between onset and C-rate are observed at a given temperature and loading. Additionally, experiment uniquely shows that temperature has nearly double the effect on plating onsets for the higher loading electrodes (Fig. 2b-ii) than lower loading electrodes (Fig. 2b-i), as indicated by the larger vertical shift in the curves. Physically, this could mean that for the thin electrodes with onsets above 50% SOC, the accumulation of bulk Li_1C_6 and its low open-circuit potential throughout the electrode promotes lithium deposition regardless of improved Li transport or intercalation kinetics with temperature. In the thicker electrodes with plating at low SOC, the strong temperature effect suggests that porous electrolyte Li^+ transport determines Li plating by controlling the uniformity of graphite lithiation and therefore the SOC at which Li_1C_6 forms at the graphite|separator interface²⁴. These explanations are consistent with optical microscopy that shows Li plating first appears on top of gold-colored Li_1C_6 particles²⁷.

In general, the EChem model (dashed lines, Fig. 2b) accurately captures the onset of lithium plating with less than 5% SOC error. Model predictions matched experiment best by slightly modifying graphite properties from those previously reported^{9,24}, such as lowering the activation energy for solid-state diffusion from 30 kJ/mol to 15 kJ/mol (Fig. S9). We believe this indicates a need to explicitly determine the diffusion coefficient as a function of lithiation and temperature. At high temperatures, loadings, and charge rates (2b-ii, upper right), the model predicts lithium plating 5-10% SOC earlier than measured, and for low loadings (2b-i), the model predicts larger temperature sensitivity than measured. This could be related to changes in SEI composition/resistivity with elevated temperatures, complex graphite phase behavior, or diffusion enhancement with rate²⁸, none of which are captured by the model. Another important insight from the experiments is that, like the model predicts, the profile of the irreversible Li curve is similar near the plating onset (Fig. 2c) regardless of rate, temperature, and loading, indicating some universal physics of Li plating behavior. Additionally, the experiment uniquely shows that the higher-loading electrode (blue shades) tends to promote faster accumulation of irreversible Li, which is likely due to higher local current densities near the separator that promote faster, more dendritic – and thus more irreversible – Li plating. The low graphite lithiation (SOC) at these onsets could also promote more rapid Li metal dissolution, which supports Li^+ re-intercalation into the graphite after charge^{29,30}, making remaining Li deposits more susceptible to electrical isolation.

Given that the plating onset varies somewhat linearly with changes in other variables, we propose an empirical equation, separate from the physics-derived EChem model, to relate the variables as a step towards data-driven Li plating models. The plating onset SOC, y , is written as a linear function of the C-rate (c), loading (x), and temperature (T), with coefficients α , β , and γ^* respectively, and intercept ε (Eqn. 1). The $(1-y)$ correction for γ within γ^* was added to account for the variable temperature effect

with loading in Fig. 2b, noting that T has a smaller impact for plating onsets at higher onset SOC. Rearrangement to solve for y yields Eqn. 2. Applying the empirical fitting to the 20 $[y, c, x, T]$ plating onset pairs with 4 parameters unsurprisingly gives a much-improved onset prediction compared to the Newman model (Fig. 3a), and nearly 60% reduction in the residual sum of squared errors (SSE). Fig. 3b highlights the benefits for interpreting the data using an analytically differentiable equation, which can provide heuristics for how Li plating should vary with design parameter changes. Starting from 30°C, 3.1 mAh/cm², and 4C rate, for example, a 1C rate increase would cause a 9% SOC earlier plating onset and a 1°C increase would postpone the onset 0.7% SOC. This analysis complements recent work that found a linear correlation between the plating onset and electrode ionic resistance, elucidating the effects of electrode structure and loading³¹. We also investigated the model's predictive capabilities by studying a graphite electrode with identical composition but 3.75 mAh/cm² loading, well above the previous experimental range, and observe that it impressively predicts the plating onset within 4% SOC at moderate rates and temperatures (Fig. 3c). Finally, the equation is useful for visualizing battery design tradeoffs, and Fig. 3d shows the charging temperature required to avoid plating for a constant-current (CC) charge to 40% SOC for various combinations of rates and loadings. Additional visualizations of the empirical fitting and a discussion of its limitations are in Fig. S10 of the Supplementary Information.

$$(1) y(c, x, T) = \alpha c + \beta x + \gamma^* T + \varepsilon \quad \text{where } \gamma^* = \gamma (1 - y)$$

$$(2) y(c, x, T) = \frac{\alpha c + \beta x + \gamma T + \varepsilon}{1 + \gamma T}$$

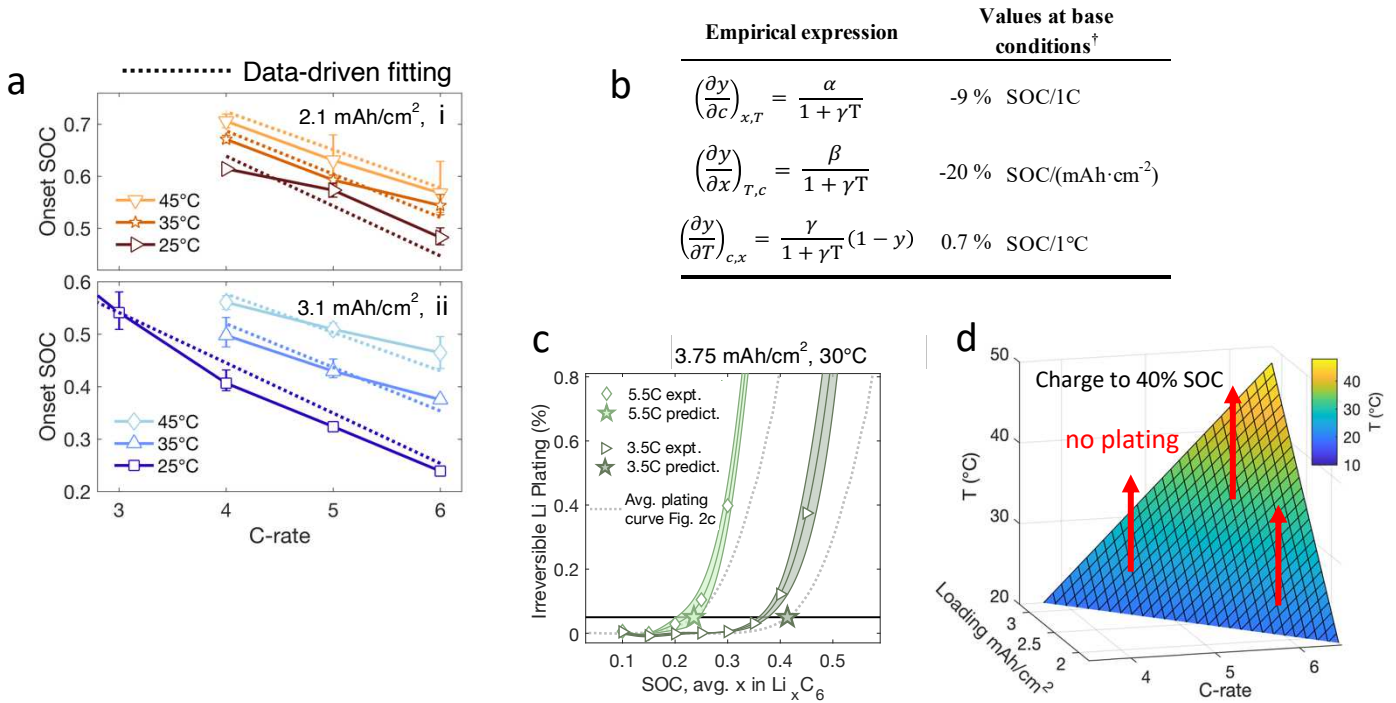


Fig. 3 | Utility of data-driven fitting for battery design. **a**, Data-driven fitting with a simple non-linear equation compared with experimental Li plating onsets. **b**, Using the empirical fitting to isolate the effect of changing C-rate (c), loading (x), and temperature (T) on the lithium plating onset (y). [†]Partial derivatives are evaluated at 30°C, 3.0 mAh/cm², and 4C with fitted model parameters $\alpha = -0.16$ SOC/1C, $\beta = -0.315$ SOC/mAh·cm⁻², $\gamma = 0.025$ (°C)⁻¹, and $\varepsilon = 1.70$ SOC. **c**, The fitting predicts the lithium plating onset at 0.05% Li plating for a graphite electrode with loading of 3.75 mAh/cm², outside the loading range of the study in Fig. 2, within 4% SOC at moderate temperatures (30 °C) and rates (3.5-5.5C). The dotted lines are the average universal Li plating curve for 3.1 mAh/cm², shifted by the predicted onsets. **d**, Visualizing the charging temperature required to avoid plating if charge to 40% SOC is desired, a potential empirical fitting application.

Electrolyte discovery to reduce irreversible Li

Next, we analyze electrolyte formulations using the validated SOC-sweep to assess their ability to reduce irreversible Li plating. Abundant literature demonstrates that fluoroethylene carbonate (FEC) at additive or co-solvent levels can lessen dead Li in Li metal and other battery chemistries^{12,32}, but few have studied its impact on extreme charging of graphite anodes. Figure 4a shows the effect of swapping ethylene carbonate (EC) for varied weight percent (wt%) FEC on irreversible plating. The notable shift in the curve from 0% to 5% FEC indicates a delayed onset of lithium plating, and the decreasing slopes with increasing FEC suggest a beneficial concentration effect for reducing dead Li. This observation arises despite decreasing bulk electrolyte conductivity with increasing FEC (Fig. S11), which led us to hypothesize that enhanced interfacial properties or fractional plating reversibility may alternatively explain this result.

To systematically explore whether Li plating reversibility plays a role in improved performance with FEC, we sought a rigorous high throughput method to quantify the value at conditions relevant to fast charging. The estimation of plating reversibility on graphite at standard SOC (below 100%) and ambient temperatures is challenging due to the rapid dissolution of reversible Li deposits that supports Li^+ re-intercalation into the graphite.^{27,29,30} A workaround to this is to study plating during graphite overcharge (above 100% SOC)^{33,34}, which has also emerged in the context of hybrid graphite/lithium anodes³⁵⁻³⁷, but reversibility estimates have only been reported at low current rates ($< 0.5\text{C}$) and/or are deduced from qualitative voltage plateau transitions.

The framework we apply to carefully and efficiently estimate the reversibility of Li plating (η) on graphite during fast charge is summarized in Figure 4b. After formation cycling, the first step is to estimate the coulombic efficiency for graphite intercalation (CE_{int}) without lithium plating (Table S4). Next, that same cycle is repeated with an added overcharge step to induce a known capacity of lithium plating, P . The capacity lost due to lithium plating is then isolated by subtracting the capacity loss from intercalation from the total capacity loss from the overcharge cycle, which allows the calculation of η (Fig. 4b, equation). Repeating the overcharge cycle 4x on the same cell gives reproducible calculated reversibility values for the first three overcharge cycles, increasing confidence in the method and allowing error bar estimation with a single cell (see Fig. S12).

Figure 4c shows the calculated lithium plating reversibility for various FEC-containing electrolytes when the overcharge amount is varied at a fixed 4C rate (left) and the deposition rate is varied at 20% overcharge (right). The plating overcharge amount is defined as the percentage of total graphite capacity (here, 3.1 mAh/cm^2) that the electrode is charged beyond complete lithiation. For all conditions, FEC-free electrolyte exhibits the lowest η , ranging between 74-91%, and for all electrolytes, the expected trends of decreasing η with increasing plating amount and rate are apparent. The beneficial concentration effect in FEC-containing electrolytes from Fig. 4a is again observed with the exception of low-rate or low-amount conditions, circled in Fig. 4c. We ascribe this observation to plating occurring primarily beneath the graphite SEI³⁸, which we believe has similar composition across concentrations due to overlapping differential capacity curves during the first graphite intercalation (Fig. 4d) when the majority of SEI is formed.

Finally, we try to connect these η determined from overcharge experiments to the true η range observed during fast charging. In the latter, plated lithium is observed within microns of the graphite/separator interface^{25,39} due to developed concentration and potential gradients, but the overcharge protocol differs because it begins without gradients and thus should initially yield more uniform Li deposition, as

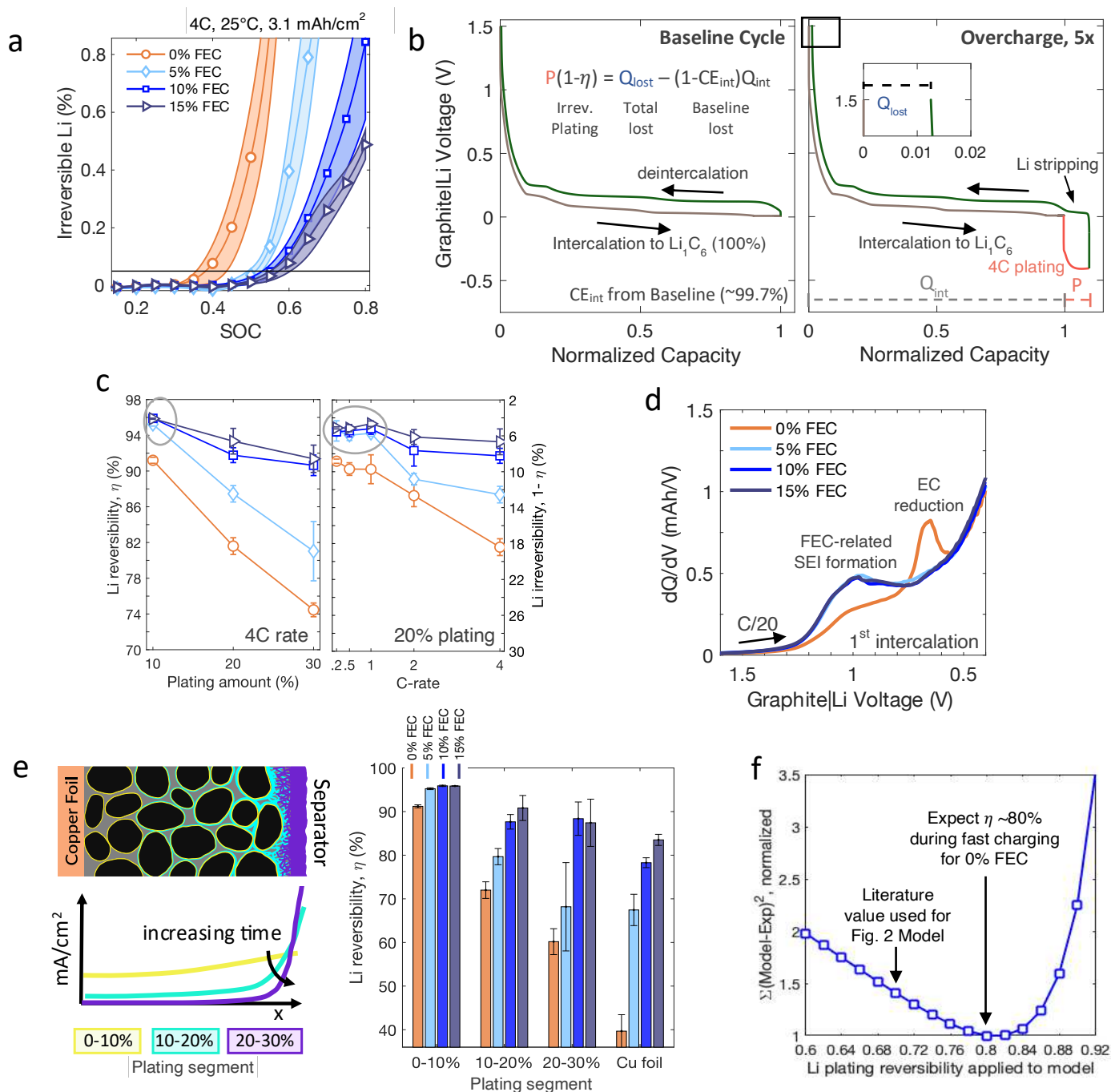


Fig. 4 | Electrolyte engineering to reduce irreversible Li plating. **a**, Irreversible Li in Graphite|Li cells using the Fig. 1 protocol for varied weight percent (X) FEC in 1.2 M LiPF₆ electrolyte, resulting in FEC:EC:EMC wt% ratios of X:(30-X):70. **b**, Overcharge protocol and equations to rigorously determine the lithium plating reversibility for high-rate plating. **c**, Li reversibility when varying the amount of 4C plating (left) and varying C-rate (right) for 20% plating, where 10% is 0.31 mAh/cm². **d**, Differential capacity curves from the first graphite lithiation. **e**, Left: Temporospatial schematic of Li plating location during 30% overcharge and sketch of associated current densities. Right: Plating reversibility by each segment for each electrolyte composition, calculated from data in (c), compared with reversibility for the same rate (4C) and plating amount (10%) on copper foil. **f**, The sum of squared errors (SSE) for Li plating onsets from experiment and the electrochemical model (Fig. 2b) across all conditions vs. the plating reversibility assumed by the model.

240 imaged at low rates³⁶. Consequently, Figure 4e is a sketch of how lithium plating likely accumulates
 241 during 4C overcharge, a hypothesis consistent with intuition about gradient development, effective
 242 porosity decreasing as Li deposits grow, and the observed decrease in η with plating amount as these

effects lead to higher local current densities and non-uniform deposits near the separator interface. To better understand the effect of location on η , an incremental plating reversibility $\Delta\eta$ for each subsequent 10% of plating is calculated directly from data in Fig. 4c (see Methods). An interesting feature arising from this analysis is that for 30% overcharge, the reversibility for the final segment of plating $\Delta\eta_{20-30}$ is drastically lower for the 0 and 5% FEC electrolytes, suggesting that the η for the 10% overcharge experiment, equivalent to $\Delta\eta_{0-10}$, is artificially high due to uniform plating deposition throughout the electrode. The 10-15% FEC samples, in comparison, show less performance decline with plating amount, perhaps due to bulk electrolyte effects such as enhanced Li^+ solvation by FEC⁴⁰. As depicted by the Fig. 4e diagram, this last plating segment may occur in a planar manner after protruding through the graphite SEI, with growth constrained by the separator. Thus, we might expect comparable reversibility for Li plating on a planar substrate such as copper foil, and indeed similar trends are observed using identical plating amounts and current densities (Fig. 4e, right, see Fig. S13 for details).

Despite the illustrative range of possible plating reversibilities, it remains unclear which is most representative of plating under standard charging conditions, i.e. which can best predict irreversible Li with models or quantify electrolyte improvements. Leveraging our comprehensive experimental and modeling datasets for the 0% FEC electrolyte, we determine the single η that minimizes the plating onsets error across all conditions (Fig. 4f, Figs. S7-S8). The η from this analysis is 80%, but most importantly, the SSE divergence above 90% provides strong evidence that the plating reversibility does not exceed this value in practice, highlighting the need for careful interpretation of overcharge plating data. Looking at 0% FEC data in Fig. 4e, $\eta=80\%$ is between the values for $\Delta\eta_{0-10}$ and $\Delta\eta_{10-20}$, suggesting that – if an average of the $\Delta\eta_{0-10}$ and $\Delta\eta_{10-20}$ values are representative of true plating reversibility – this electrolyte would produce 2-3x as much irreversible lithium ($1-\eta$) compared with the FEC electrolytes (for 5-15% FEC, average $\Delta\eta$ are 88-93%). Holistically, this evidence suggests that η is an important electrolyte/interphasial design property for systems susceptible to Li plating. Going forward, we expect the technique of Fig. 4b to be useful for characterizing additional electrolytes and assessing innovative methods to mitigate irreversible plating such as separator design⁴¹.

Full-cells and titration validation

The last step of this workflow is to confirm that the half-cell results are transferrable to commercial full-cell chemistries, which instead require a porous, high-voltage cathode material with limited lithium inventory. To compare lithium plating behavior across electrolyte compositions, a Graphite| $\text{LiNi}_{0.5}\text{Mn}_{0.3}\text{Co}_{0.2}\text{O}_2$ (NMC532) was cycled 140 times, alternating 5 moderate 1C CCCV (constant current constant voltage) charging cycles to 4.2V, holding until C/5 current, with 2 6C CCCV fast charging cycles to 4.2V, holding until 80% capacity. We selected this protocol to help isolate fast charging-related capacity loss, expected only during the 6C cycles, from other cell aging effects such as FEC degradation⁴². Figure 5a shows that the 5-15% FEC full-cells, similar to half-cells, outperform the FEC-free electrolyte, undergoing on average only about 30% of the capacity fade over the 100 1C cycles, with similar 6C CCCV charge times compared to 0% FEC (Figs. S19-20). The 2% FEC electrolyte, included for the common use of FEC as an additive, performed only slightly worse than the higher concentrations. From our Li reversibility analysis, the lack of a clear concentration effect on performance may indicate small amounts of plating occurring mostly beneath the FEC-derived SEI. It may also indicate the importance of SEI in delaying the plating onset SOC, which is seen in Fig. 4a and suggested by others⁴³ to explain better rate performance with an artificial graphite SEI coating. Significant sample variability is expected due to the heterogeneous nature of lithium plating and is depicted by the representative error bars obtained from replicate trials on multiple cells.

291 We then use the cycling data to quantify degradation from fast charging and compare results with Li
 292 titrations of the extracted electrodes. Others have reported that irreversibly plated lithium is linearly
 293 correlated to cell capacity loss⁴⁴, so we expect the abrupt capacity changes after the 6C cycles (Fig. 5a,
 294 box) to correlate with titrated Li capacity from mass spectrometry titration (MST). MST¹³ accurately
 295 quantifies the combined H₂-evolving species on graphite such as isolated ‘dead’ Li⁰ and inactive Li_xC₆
 296 with exceptional resolution (see Methods). However, the titrated Li slightly exceeds the capacity loss for
 297 most of the 0% FEC samples despite controls that show minimal Li_xC₆ contribution, suggesting that
 298 plating is not fully quantified by this metric (Fig. S26). The source of this error may be visualized in the
 299 1C charging profiles for a representative cell in Fig. 5b-i, recalling that 1C cycle 5 is followed by 6C

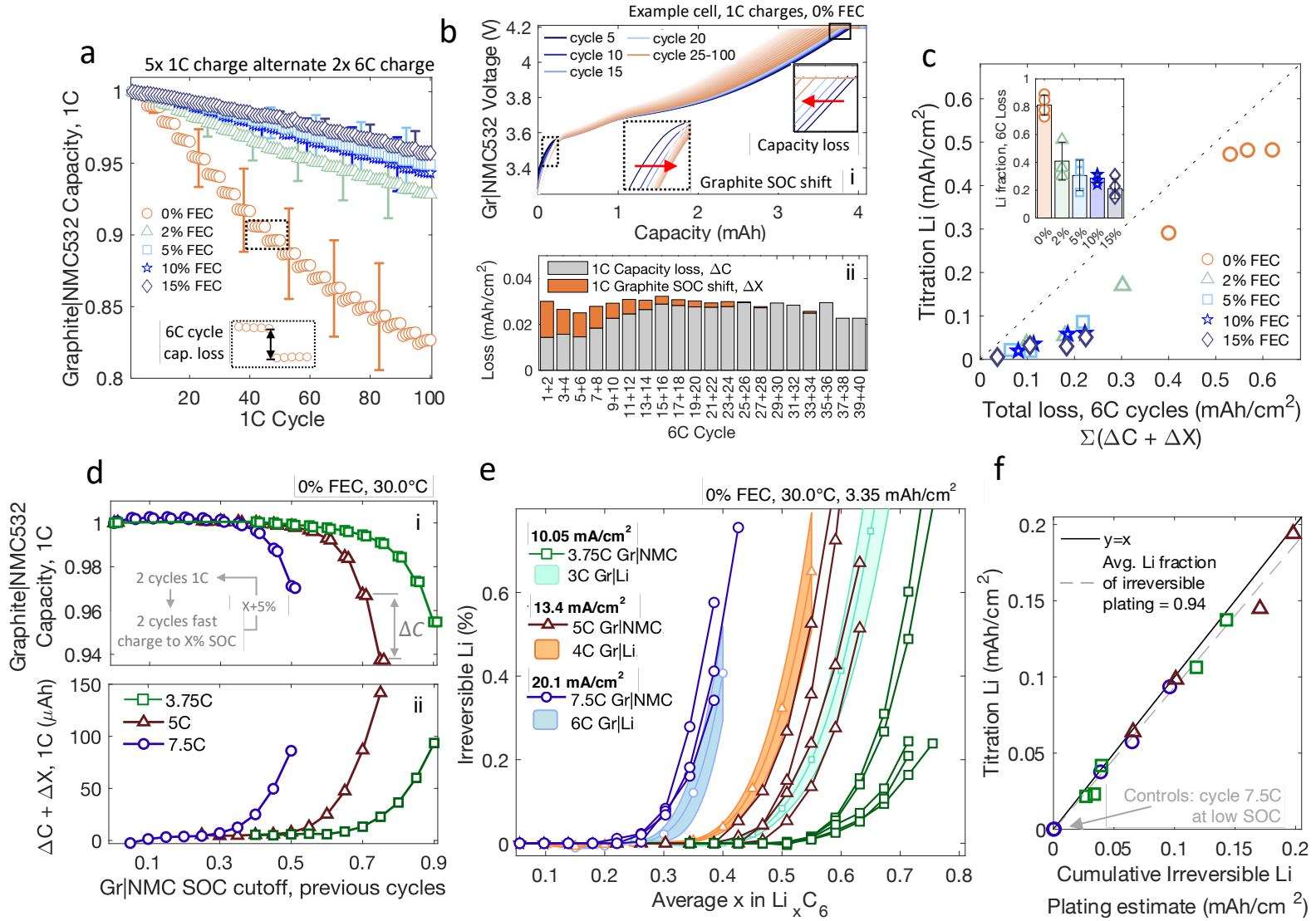


Fig. 5 | Graphite|NMC532 full-cells testing with dead Li quantification and comparison with Graphite|Li

a, 1C discharge capacity normalized to the initial (Cycle 1) value vs. cycle number, with cells undergoing two cycles of 6C CCCV to 4.2V charging to 80% SOC after five 1C cycles. **b**, i) Representative 1C charging profiles throughout cycling. Insets show how the profile shifts during cycling. ii) Loss quantified from capacity change and graphite SOC shift. The data for 6C Cycles 1+2 is determined by analyzing 1C Cycles 3-5 (before 6C) and 7 (after, see Methods for details). **c**, Titrated Li (Li⁰ and Li_xC₆) vs. the sum of the data in b-ii for all cells tested in (a). **d**, Characterizing irreversible Li in full-cells by monitoring the normalized 1C discharge capacity with intermittent 2 cycles of constant-current fast charging to progressively higher SOC. **e**, Comparing irreversible lithium on graphite with NMC (connected points, individual cells) and Li (shaded regions, averaged 3 cells) counter electrodes as a function of the average graphite lithiation at the end of charge. The full-cell SOC is converted to average graphite lithiation as described in the methods. **f**, Titrated Li vs the total irreversible Li plating estimates for the graphite electrodes extracted from the Gr|NMC cells in (e).

cycles 1 and 2 then 1C cycle 6, and that 1C cycle 10 is followed by 6C cycles 3 and 4, and so forth. The profiles show that for the first few fast charging cycles, the voltage segment corresponding to early graphite lithiation shifts to the right (dashed box). Physically, the shift indicates a change in the electrode potential windows during charge and the removal of additional cyclable lithium⁴⁵ from the graphite to compensate lithium losses from plating. Thus, we believe this graphite SOC shift should estimate losses not captured by the 1C capacity loss, which conversely manifests by the high-voltage capacity shifting to the left (solid box). The SOC shift (ΔX) and capacity loss (ΔC) are reported for each pair of 6C fast charging cycles in Fig. 5b-ii (see Methods for detailed calculation). The combined loss for each pair of cycles is about the same, which is reasonable because i) the amount of loss per pair is small, ~1% of the total capacity, and ii) the cell aging that might promote increased plating over time is counterbalanced by increasing CCCV charge times, which lowers the average C-rate (Fig. S19). The graphite SOC shift contribution decreases from about 50% of losses for 6C Cycles 1-2 to ~0% for Cycles 25-26 and beyond as the residual lithium in the graphite is consumed, highlighting the importance of this metric for accurate early plating quantification. Fig. S23 shows Fig. 5b-ii for all cells, an impressive visualization that indicates accurate loss quantification with single cycle resolution.

Fig. 5c shows significantly less titrated Li for the FEC electrolyte cells compared to the 0% FEC cells, as anticipated from Figs. 4 and 5a electrochemical measurements and electrode images (Fig. S24). There is also a strong correlation between the sum of the 6C losses (from Fig. 5b-ii) and titrated Li. For the 0% FEC electrolyte, the fraction of the loss accounted for by titrated Li is about 81% (Fig. 5c inset), comparable to other studies of dead Li using similar electrolytes^{12,13}. This leads us to suspect that the majority of the 6C losses are indeed due to irreversible Li plating, but note that this metric may include losses from other fast-charging degradation such as SEI formation or electrode active material loss. The Li fraction with FEC is lower and decreases slightly from about 40% to 20% with increasing concentration, again highlighting the potential FEC advantage for avoiding metallic Li buildup during cell malfunction. Still, these values are notably higher than the ~10% fractional dead Li that others have observed for slow Li deposition on Cu for similar FEC electrolytes^{12,32,46}, emphasizing phenomena unique to fast charging and the need to understand loss mechanisms besides dead Li formation.

Finally, the titration results unveil a route for estimating irreversible Li as a function of SOC in full-cells to allow direct comparison with half-cell results. The combined 1C capacity loss and 1C graphite SOC shift ($\Delta C + \Delta X$) was a strong predictor for titrated Li for the 0% FEC electrolyte, so we then designed a protocol alternating two 1C charge cycles with two fast charging cycles to X% SOC, where X is increased by 5% for each iteration (Fig. 5d-i). Two cycles of each step were performed to benefit the technique sensitivity and reliability (see Fig. S28). The 1C capacity changes between fast charging steps (ΔC) correspond to losses from only those X% SOC cycles. Similarly, the 1C graphite SOC shift (ΔX) is calculated for each X% SOC fast charge step, and the combined loss is shown in Fig. 5d-ii, as in our previous analysis. This metric is shown for representative cells at various C-rates, and the x-axis denotes the SOC cutoff of the previous 2 fast charge cycles that are analyzed. For the full-cells, the rates and SOC are defined with respect to the nominal 3-4.2V C/10 charge capacity, and were selected so that identical graphite current densities are applied for comparison with 3C to 6C rates in the half-cells (see Supplementary Information for discussion).

We then transform the data in Fig. 5d-ii to estimate irreversible Li plating in full-cells and provide a direct comparison with the half-cells in Fig. 5e. The transformation entails i) subtracting baseline losses observed for fast charging at low SOC prior to the plating onset, as in Fig. 1b (Fig. S30), ii) normalizing the loss to the active graphite capacity, as in Fig. 1c, and dividing by 2 to account for 2 cycles to each SOC, and iii) converting the x-axis from full-cell SOC to graphite lithiation (avg. x in Li_xC_6) by differential voltage profile analysis (see Fig. S32). We assume that 100% of the baselined $\Delta C + \Delta X$ data

corresponds to irreversible Li plating capacity. A striking similarity is the shape of the Gr|Li and Gr|NMC curves, which extends our hypothesis from Fig. 2c of universal physics for Li plating regardless of counter electrode selection. Another interesting observation is that the spacing of the Gr|Li curves have a similar C-rate dependence as those of the Gr|NMC, which reveals a route for empirically scaling the half-cell data to predict full-cell behavior with limited full-cell measurements (Fig. S33). Even without this adjustment, however, the half-cells show average Li plating onset SOC (defined again as 0.05% irreversible Li) within 3% of full-cells for the 20.1 mA/cm² rate and within 6% for 13.4 mA/cm², suggesting the Fig 2a-b Gr|Li measurements at the higher current densities (4C and above) are the most translatable for full-cells. We also offer some physical explanations for the plating onset differences based on prior modeling in the supplementary information.

The highlight of this analysis is that we demonstrate a validated, highly sensitive, in-situ method for quantitative Li plating estimation in full-cells. As the final step of technique verification, the graphite electrodes were titrated for comparison with the cumulative irreversible Li estimated for each cell (Fig. 5f), determined by summation of the $\Delta C + \Delta X$ values of Fig. 5d-ii for each curve after the described baselining. The strong linear correlation with near unity slope further suggests that the method accurately predicts plating amounts and estimates that, on average, 94% of irreversible Li plating exists in the form of electrically isolated Li⁰ and other titration Li, with the remaining 6% as Li⁺-containing SEI species. The application of this protocol for electrolyte engineering in full-cells should be investigated in future works, but we note that this 1.2 M LiPF₆ in 3:7 EC:EMC electrolyte offers favorable Li detection properties and is well-suited for immediate subsequent studies. There is vast opportunity to quantify the effects of electrode porosity, loading, temperature, composition, and heterogeneity on Li plating to inform cell manufacturing, quality control, and battery operation.

Conclusions and Outlook

Lithium plating is a nearly universal challenge for battery performance and operation, but its difficulty to detect has limited robust experimental studies. We have developed and verified high-throughput cycling techniques to quantify lithium plating in-situ in Graphite|Li and Graphite|NMC cells, and the abundant data have led to physical insights of plating behavior, electrochemical modeling improvements, cell design heuristics, routes toward data-driven plating models, and electrolyte engineering strategies. Going forward, we believe that widespread reporting of irreversible Li plating curves and onset SOC will help quantify the tradeoffs of novel battery design or operation approaches for fast charging, as well as lead to improved fundamental understanding. We hope these techniques are employed by academic and industry researchers and continually adapted to further reduce experiment time, consider battery aging effects, transfer effectively to other cell formats, and study nascent battery chemistries.

Methods

Materials. Electrolytes were made with ethyl methyl carbonate (EMC), ethylene carbonate (EC), fluoroethylene carbonate (FEC), and lithium hexafluorophosphate (LiPF_6) from Gotion Inc and used within a week of preparation. Composite graphite electrodes were obtained from the Argonne National Laboratory CAMP facility with 91.83 wt% Superior Graphite SLC 1506T, 2 wt% Timcal C45 carbon, 6 wt% Kureha 9300 PVDF binder, 0.17 wt% Oxalic Acid on Cu foil (10 μm). Various combinations of [thickness, loading, porosity] were used based on application and availability, A1 = [47 μm , 2.1 mAh cm^{-2} , 37.4%], A2 = [70 μm , 3.1 mAh cm^{-2} , 38.2%], A3 = [70 μm , 3.35 mAh cm^{-2} , 34.4%], A4 = [85 μm , 3.75 mAh cm^{-2} , 35.4%]. Plating onset and temperature experiments (Figs. 1-2) used anodes A1 and A2. Plating reversibility experiments (Fig. 4) used A2. Full-cell plating experiments and Full-cell/half-cell validation (Fig. 5) used A3. Empirical fit prediction testing (Fig. 3c) used A4. The composite $\text{LiNi}_{0.5}\text{Mn}_{0.3}\text{Co}_{0.2}\text{O}_2$ cathode was 90 wt% Toda NMC532, 5 wt% Timcal C45 carbon, 5 wt% Solvay 5130 PVDF binder, with 2.8 mAh cm^{-2} and targeted P:N ratio 1:1.2 with anodes A2-A3, 71 μm coating on 20 μm Al foil, 35.6% porosity. All electrodes were dried at 120°C under vacuum overnight before transferring directly to the glovebox.

Hohsen CR2032 coin cells were used for all experiments, with 30 μL total electrolyte added quickly in 3 separate 10 μL aliquots to ensure uniform wetting while avoiding evaporation. Graphite electrodes were 15 mm diameter punches, paired with either 14 mm dia. Li foil (0.7 mm thickness, MTI Corp) or 14 mm dia. NMC and separated by a single 18 mm dia. Celgard 2500 separator (25 μm monolayer polypropylene). All assembly/disassembly was performed in an argon-filled glovebox with $\text{O}_2 < 1.0$ ppm, $\text{H}_2\text{O} < 0.5$ ppm. Electrochemical testing used Biologic MPG-200, VMP3, and BCS-810 potentiostats with CCH-8 coin cell holders at temperature control in Thermotron environmental chambers. Cycling protocols were implemented with Biologic's EC-Lab software.

SOC-sweep testing for Graphite|Li cells (Figs. 1, 2, 3c, 4a). One slow formation cycle entails C/10 intercalation to 0.01 V and C/5 deintercalation to 1.5 V with 5-minute rest between each step. The experimental graphite capacity is determined from the discharge capacity of the 3rd and final C/10 formation cycle and used to set the C-rates and SOC cutoffs for subsequent cycling. We refer to graphite intercalation as 'charging' and deintercalation as 'discharging' for consistency with language used for full-cell commercial lithium-ion batteries, even though the intercalation process is spontaneous in the Graphite|Li cell configuration. Next, each cell underwent 5 fast formation cycles of 4C charge to 10% SOC and C/5 discharge to 1.5V with 15-minute rest between current steps (see Fig. S2). Last, the cell undergoes the SOC-sweep cycling in which the charge capacity is increased 5-10% SOC for each subsequent cycle, with each charge step alternated with C/5 discharge to 1.5V, and a 30-minute rest between current steps. The SOC window and step size was selected based on the expected plating onset SOC; for later expected onsets, a step size of 10% was selected to cover large SOC range while minimizing experiment time (see Table S2). For high-temperature experiments, the oven temperature was increased from 25°C to the target temperature during the 5 fast charging formation cycles. For Fig. 4a comparing electrolyte compositions, the first formation cycle used C/20 instead of C/10 to clearly articulate dQ/dV features, seen in Fig. 4d. Typically 3 cells were run initially at each condition in Figs. 1, 2, 3c, and 4a, but the number of cells reported varies between 2 and 5 (e.g., see Fig. 2a, bottom left of each panel). An additional set of 2-3 cells may have been run for better data statistics or to make up for data that was excluded due to indicators of poor cell performance resulting from imperfections in manual cell preparation. For a description of such 'bad cells,' see Fig. S1.3.

Electrochemical Modeling (Figs. 2, 4f). Additional notes to supplement the main text model description: The universal plating reversibility was previously estimated to be roughly 70% ($\eta = 0.7$) under fast charge conditions and modest amounts of plating¹³. Irreversible lithium plating is determined from multiplying $(1 - \eta)$ by the modeled plating amount. All electrolyte transport properties are taken from Idaho National Laboratory's Advanced Electrolyte Model (AEM)⁴⁷ and use empirical fits as a

function of salt concentration and temperature²⁴. The anode and separator Bruggeman coefficient are estimated as 2.2-2.3 and 2.0, respectively, based on detailed microstructure characterization/modeling and impedance spectroscopy using a blocking electrolyte⁴⁸. The exchange current density and solid-state diffusion are estimated based on extensive fitting to electrochemical data including full-cells, half-cells, and 3-electrode test setups from within the US Department of Energy XCEL fast charge program^{9,24,25}. The exchange current density for the lithium working electrode and lithium plating within the graphite anode are both set to 10 A/m² as in our prior report¹³. The half-cell and full-cell models are written in C++ and use the SUNDIALS Suite of Nonlinear and Differentiable/Algebraic Equation Solvers⁴⁹.

Lithium plating reversibility on graphite protocol (Fig. 4b). After 3 C/10 formation cycles and determining the experimental capacity, the graphite is intercalated at C/3 to 0.01 V and held 1 h or until current drops below 10 μ A (C/500) followed by immediate C/5 discharge to 1.5V. This cycle is to determine the coulombic efficiency for complete graphite lithiation in the absence of lithium plating. The following 5 cycles are identical except after the intercalation, intentional overcharge (Li plating) occurs at the selected C-rate (0.2C-4C) and capacity (10-30% SOC), both specified relative to the experimental full graphite intercalation capacity. A representative voltage profile for this cycling protocol is provided in Fig. S14. The specific plating reversibility calculation is detailed in Fig. 4b and corresponding text.

Incremental plating reversibility calculation (Fig. 4e). The data from Fig. 4c report the plating reversibility for 10%, 20%, and 30% overcharge (η_{10} , η_{20} , η_{30}) collected with separate coin cells and these values can be algebraically manipulated to estimate the reversibility for Li deposited between 10-20% SOC (η_{10-20}) and 20-30% SOC (η_{20-30}):

(reversible plating 0-20% SOC) = (reversible plating 0-10% SOC) + (reversible plating 10-20% SOC)

$$\eta_{20}(20\% SOC) = \eta_{10}(10\% SOC) + \eta_{10-20}(10\% SOC)$$

$$\eta_{10-20} = \frac{0.2 \eta_{20} - 0.1 \eta_{10}}{0.1}$$

Similarly,

$$\eta_{20-30} = \frac{0.3 \eta_{30} - 0.2 \eta_{20}}{0.1}$$

And error bars were estimated by standard propagation of uncertainty (see text below Fig. S12).

Lithium plating on copper foil (Fig. 4e). Lithium was deposited on 15 mm Cu foil (25 μ m, MTI Corp) from a 14 mm Li metal electrode at a current density of 4C with respect to anode A2 capacity (3.1 mAh cm⁻²) for 1.5 minutes (0.31 mAh cm⁻², 10% SOC) to mimic plating at the Graphite|separator interface during the graphite plating reversibility experiments. Immediately after Li deposition, an oxidative C/5 current was applied until the cell voltage exceeded 1.0V. The capacity ratio of the current stripping and plating steps is the reported reversibility. This cycle was repeated 5 total times with 10 minutes rest in between, and the reversibility reported is an average value from cycles 3-5 (2+ cells for each electrolyte), which exhibit stabilized CE value relative to the first 2 cycles (Fig. S13).

Graphite|NMC532 full-cell electrolyte testing (Fig. 5a-c). The experimental full-cell capacity is determined from the discharge capacity of the 3rd and final C/10 formation cycle and used to set the C-rates and capacity cutoffs for subsequent cycling. One slow formation cycle entails C/10 charge to 4.2 V and C/5 discharge to 3.0 V. All full-cell cycles include 5-minute rests between current steps. Next, 20 additional formation cycles are performed with 1C charge to 4.2V and 1C discharge to 3.0 V, holding until the current drops below C/5 on discharge (~5 min). Cell performance is analyzed from the following sequence: 5 cycles of **a**) 1C CCCV charge to 4.2V, holding until C/5 (~10 min), and 1C discharge to 3.0 V holding until C/5, alternating with 2 cycles of **b**) 6C CCCV charge to 4.2V, holding

until 80% SOC (about 12 min total charge), then 1C discharge to 3.0 V holding until C/5. This sequence is repeated 20 times for a total of 100 1C cycles and 40 6C cycles. To prepare full-cells for titrations, the final step is a C/5 deep discharge down to 0.1 V to remove residual active lithium from the graphite.

Electrochemical data analysis (Fig. 5b-c), Electrode voltage (V) shifts or capacity (Q) changes in full-cells are often characterized by monitoring the capacity (x-position) at which local extrema in differential voltage curves (dV/dQ, y-axis) occur⁵⁰. Here, the dV/dQ vs. Q curve shift is alternatively calculated from the capacity at which $Q_0 \cdot dV/dQ = 1.0$ V, defined as X, where Q_0 is the initial cell capacity (Fig. S21). The graphite SOC shift (ΔX) between Cycles 5 and 6, which corresponds to 6C Cycles 1+2 in Fig. 5b-ii, is calculated with the following equation, and the subscript denotes the 1C cycle number:

$$\Delta X_{6C \text{ cycles } 1 \& 2} = (X_7 - X_5) - (X_5 - X_3)$$

This equation is used instead of $\Delta X = (X_6 - X_5)$ to account for transient behavior of the 1st 1C cycle after fast charging (here, Cycle 6) and to subtract nominal SOC shift that would also occur in 1C cycles, $(X_5 - X_3)$, reducing contributions from cell aging unrelated to fast charging. Fig. S22 provides thorough justification for this formula. Generalizing to determine ΔX that occurs for the 2 6C cycles n and (n+1) that occur between 1C cycles N and (N+1) yields:

$$\Delta X_{6C \text{ cycles } n \& (n+1)} = (X_{N+2} - X_N) - (X_N - X_{N-2})$$

For 1C cycle numbers: $N = [5, 10, 15, \dots, 90, 95]$ and
Corresponding 6C cycle numbers: $n = (2N/5) - 1 = [1, 3, 5, \dots, 35, 37]$

Similarly, the changes in 1C discharge capacity reported in Fig. 5b-ii, ΔC , are calculated by the following where C is the discharge capacity for the Nth 1C cycle:

$$-\Delta C_{6C \text{ cycles } n \& (n+1)} = (C_{N+2} - C_N) - (C_N - C_{N-2})$$

For both ΔX and ΔC , the values for 6C cycles 39&40 are assumed identical to cycles 37&38 because additional 1C cycles were not performed after the 2 final fast charge cycles.

Graphite|NMC532 SOC-sweep Li plating quantification (Fig. 5d-f). For these cells, the experimental full-cell capacity, $C_{full-cell}$, was fixed at 4.30 mAh (100% SOC, 2.80 mAh/cm², average of previous experiments) to fix the current density applied to the graphite electrodes for comparison with Graphite|Li cells. **1. Cycling Protocol.** **a)** 3x slow formation cycles 3.0-4.2V as described above. **b)** 10x 1C formation cycles CC charge to 4.2V, 1C CCCV discharge to 3.0V hold until C/20. Holding until C/20 was selected to minimize the graphite lithiation at the start of charge for the best comparison with Graphite|Li cell measurements. **c)** 1x cycle C/10 charge to 4.2V, 1C discharge to 3.0V hold until C/20. The charging step is used for dV/dQ analysis to determine the active graphite capacity and graphite lithiation at the start of charge (Fig. S32). **d)** Cell performance was analyzed from the following sequence (see Fig. S27 for representative voltage profiles during this protocol): 2 cycles of **i)** 1C CCCV charge to 4.2V, holding until C/5 (~10 min), and 1C discharge to 3.0 V holding until C/20, alternating with 2 cycles of **ii)** fast charge at the specified C-rate constant-current until X% SOC, then 1C discharge to 3.0 V holding until C/20 and **iii)** repeating from sequence i) except increasing the fast charging SOC cutoff of ii) by 5%. After the final set of fast charging cycles, 2 additional 1C cycles are performed. **iv)** C/5 deep discharge to 0.1V to prepare for titrations. **2. Data analysis.** **a)** The graphite SOC shift ΔX and capacity loss ΔC for each pair of fast charging (FC) cycles was calculated by taking the difference of the 2nd cycle of each pair of 1C cycles. Only the 2nd cycle was analyzed due to transient capacity and

coulombic efficiency behavior for the 1st 1C cycle of each set after fast charge (Fig. S28) . Inspired by the analysis described for the 140-cycle full-cell methods above:

$$\begin{aligned}\Delta X_{fast\ charge\ at\ XC\ to\ X\% \ SOC} &= (X_{2nd\ 1C\ cycle\ after\ FC} - X_{1C\ cycle\ before\ FC}) \\ -\Delta C_{fast\ charge\ at\ XC\ to\ X\% \ SOC} &= (C_{2nd\ 1C\ cycle\ after\ FC} - C_{1C\ cycle\ before\ FC})\end{aligned}$$

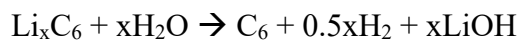
Note: in contrast to the 140-cycle full-cell equations for ΔX and ΔC , here there is no correction term that subtracts losses for 1C aging. **b)** This is because for the next analysis step, to estimate irreversible Li plating, the $\Delta C + \Delta X$ data from part **(a)** (seen in Fig. 5d) is baselined to subtract losses from aging that are not related to lithium plating. This process is illustrated and discussed thoroughly in Fig. S30. **c)** Finally, to convert full-cell SOC at the end of charge (x-axis, Fig. 5d) to graphite lithiation at end of charge (x-axis, Fig. 5e), the following equation is used:

$$x\ in\ Li_xC_6 = x_{initial} + SOC_{full-cell} \cdot \frac{C_{full-cell}}{C_{active_graphite}}$$

Where $x_{initial}$ is the initial graphite lithiation at the beginning of charge and $C_{active_graphite}$ is the active graphite capacity, both determined from dV/dQ analysis (Fig. S32). Uncertainty propagation analysis indicates that the error induced by this transformation is no larger than 1% lithiation (see SI).

Electrode extraction, imaging, mass-spectrometry titration, and titration calibrations (Fig. 5c,f). Graphite electrodes from full-cell experiments were extracted with a Hohsen Coin Cell Disassembling Tool in the glovebox and imaged with a wireless handheld microscope (TAKMLY) before transferring to individual 6 mL vials (Metrohm). The vials were placed under active vacuum for 5 minutes before crimp-sealing the septum caps. Electrodes were extracted within 24 h of cycling completion and were stored in the glovebox for up to 3 days before titration. Rinsing the electrodes 2x with dimethyl carbonate before vial storage was found to have minimal effect on dead Li measurements, so the majority of samples were not rinsed (Fig. S26).

The Ar-filled sample vials were removed from the glovebox, quenched with 0.5 mL of nitrogen-sparged deionized water, swirled for 10 seconds, and then attached to the mass spectrometry titration (MST) system using a novel syringe needle attachment featuring an adapter (Valco, part # ZBUMLPK) from 1/16" stainless steel tubing to Luer-lock (Fig. S15). The MST system draws 2 mL of the vial headspace every 2 minutes, refilling the balance with ultra-high purity Argon, using a constant system pressure of 1030 ± 10 Torr. After about 40 minutes, or when the H₂ signal ($m/z = 2$) had decayed to its initial value (Fig. S16), the next vial was attached. This new vial-swapping design along with smaller vial volume resulted in a three-fold throughput increase from our previous work¹³, and the signal strength suggests that 50 ng of Li metal (equivalent to 0.2 μ Ah total capacity) can be confidently quantified with each headspace sample precise to 10 ng (Fig. S17). The calibration process that quantifies the linear relationship between the H₂ signal and the partial pressure of H₂ is detailed in the Supplementary Information discussion for Fig. S18. To safely and precisely generate small quantities of H₂ in the 6 mL vials, graphite electrodes were formed and lithiated to known SOC (10-30%) in half-cells, extracted as detailed above, cut into pieces with known mass fractions of the entire 15 mm electrode, and titrated, assuming the complete conversion of the following reaction:



The amount of titrated Li in the manuscript is presented as a capacity by converting the moles of H₂ assuming 1 mol oxidizable Li species per 0.5 mol H₂, and 1 mol e⁻ per mol Li.

Even in the absence of lithium plating, cycled graphite electrodes are expected to have nonzero

titrated Li due to the presence of residual $\text{Li}_x\text{C}_6^{13}$ that is either electrically isolated or not fully removed during the deep discharge step. This nonzero amount was quantified with controls for each type of experiment and subtracted from the values reported in Fig. 5. For Fig. 5a-c experiments, the value was $0.012 \pm 0.002 \text{ mAh/cm}^2$ (see Fig. S25), and for Fig. 5d-f experiments it was $0.019 \pm 0.001 \text{ mAh/cm}^2$ (Fig. S31), both of which are $<1\%$ of the total graphite lithiation capacity of 3.25 mAh/cm^2 .

Acknowledgements

This work was largely supported by the Vehicle Technologies Office of the U.S. Department of Energy under the XCEL Fast Charging Program (eXtreme Fast Charge Cell Evaluation of Lithium ion Batteries, XCEL). Part of this work was authored by the National Renewable Energy Laboratory, operated by the Alliance for Sustainable Energy, LLC, for the U.S. Department of Energy (DOE) under Contract DE-AC36-08GO28308. H.K.B., D.E.B., and E.J.M. acknowledge support from the National Science Foundation Graduate Research Fellowship Program under Grant DGE 1106400. T-Y.H. gratefully acknowledges support collectively from both Ministry of Education in Taiwan and UC Berkeley College of Chemistry through the Taiwan Fellowship Program. The authors thank S. Trask, A. Jansen, A. Dunlop, and B. Polzin from the Argonne National Laboratory Cell Analysis, Modeling, and Prototyping (CAMP) facility for providing laminate electrodes used in the study. Z.M.K. thanks Jeffrey Heo for assistance with Fig. 4e design.

Author Contributions

Z.M.K. conceived ideas, performed experiments, developed methods, wrote analysis code, wrote manuscript and SI. **B.M.W.** developed Fig. 4 methods and analysis with Z.M.K. and provided continuous project and manuscript feedback. **A.V.** and **A.M.C.** performed EChem modeling simulations and wrote corresponding manuscript/SI sections. **T-Y.H.** helped Z.M.K. build titration syringe attachment. **H.K.B.** helped experiment design for Li plating on copper and electrolyte conductivity measurements. **M.J.C.** and T-Y.H. provided feedback and assistance with titrations. **D.E.B.** and **E.J.M.** provided project feedback, troubleshooting ideas, and mentorship. **A.M.C.** also conceived Fig. 2 experiments with Z.M.K., led EChem model modifications, and provided continuous project feedback. **B.D.M.** was lead project supervisor, conceived ideas, and was primary manuscript editor. All authors edited and provided feedback on manuscript.

Note: The views expressed in this Letter do not necessarily represent the views of the DOE or the U.S. Government. The U.S. Government and the publisher, by accepting the article for publication, acknowledge that the U.S. Government retains a nonexclusive, paid-up, irrevocable, worldwide license to publish or reproduce the published form of this work, or allow others to do so, for U.S. Government purposes. The authors declare no competing financial interest.

References

1. Rashingkar, G. & Frost & Sullivan. *Global Li-ion Battery Materials Growth Opportunities*. <https://www.marketresearch.com/Frost-Sullivan-v383/Global-Li-ion-Battery-Materials-14856305/> (2021).
2. Zhang, S. S., Xu, K. & Jow, T. R. Study of the charging process of a LiCoO₂-based Li-ion battery. *J. Power Sources* **160**, 1349–1354 (2006).
3. Tobishima, S. I. & Yamaki, J. I. A consideration of lithium cell safety. *J. Power Sources* **81–82**, 882–886 (1999).
4. DNV-GL and Arizona Public Service. *McMicken Battery Energy Storage System Event Technical Analysis and Recommendations*. <https://www.aps.com/-/media/APS/APSCOM-PDFs/About/Our-Company/Newsroom/McMickenFinalTechnicalReport.ashx?la=en&hash=50335FB5098D9858BFD276C40FA54FCE> (2020).
5. Arora, P., Doyle, M. & White, R. E. Mathematical Modeling of the Lithium Deposition Overcharge Reaction in Lithium-Ion Batteries Using Carbon-Based Negative Electrodes. *J. Electrochem. Soc.* **146**, 3543 (1999).
6. Tang, M., Albertus, P. & Newman, J. Two-Dimensional Modeling of Lithium Deposition during Cell Charging. *J. Electrochem. Soc.* **156**, A390 (2009).
7. Yang, X. G., Ge, S., Liu, T., Leng, Y. & Wang, C. Y. A look into the voltage plateau signal for detection and quantification of lithium plating in lithium-ion cells. *J. Power Sources* **395**, 251–261 (2018).
8. Ren, D. *et al.* Investigation of Lithium Plating-Stripping Process in Li-Ion Batteries at Low Temperature Using an Electrochemical Model. *J. Electrochem. Soc.* **165**, A2167–A2178 (2018).
9. Colclasure, A. M. *et al.* Requirements for Enabling Extreme Fast Charging of High Energy Density Li-Ion Cells while Avoiding Lithium Plating. *J. Electrochem. Soc.* **166**, A1412–A1424 (2019).
10. Campbell, I. D., Marzook, M., Marinescu, M. & Offer, G. J. How Observable Is Lithium Plating? Differential Voltage Analysis to Identify and Quantify Lithium Plating Following Fast Charging of Cold Lithium-Ion Batteries. *J. Electrochem. Soc.* **166**, A725–A739 (2019).
11. Paul, P. P. *et al.* A Review of Existing and Emerging Methods for Lithium Detection and Characterization in Li-Ion and Li-Metal Batteries. *Adv. Energy Mater.* **11**, 1–29 (2021).
12. Fang, C. *et al.* Quantifying inactive lithium in lithium metal batteries. *Nature* **572**, 511–515 (2019).
13. McShane, E. J. *et al.* Quantification of Inactive Lithium and Solid–Electrolyte Interphase Species on Graphite Electrodes after Fast Charging. *ACS Energy Lett.* **5**, 2045–2051 (2020).
14. Deng, Z. *et al.* Towards autonomous high-throughput multiscale modelling of battery interfaces. *Energy Environ. Sci.* **15**, 579–594 (2022).
15. Kang, K., Meng, Y. S., Bréger, J., Grey, C. P. & Ceder, G. Electrodes with high power and high capacity for rechargeable lithium batteries. *Science* **311**, 977–980 (2006).
16. Qie, L. *et al.* Nitrogen-doped porous carbon nanofiber webs as anodes for lithium ion batteries with a superhigh capacity and rate capability. *Adv. Mater.* **24**, 2047–2050 (2012).
17. Smith, A. J., Burns, J. C., Trussler, S. & Dahn, J. R. Precision Measurements of the Coulombic Efficiency of Lithium-Ion Batteries and of Electrode Materials for Lithium-Ion Batteries. *J. Electrochem. Soc.* **157**, A196 (2009).
18. Dahn, J. R., Burns, J. C. & Stevens, D. A. Importance of coulombic efficiency measurements in R & D efforts to obtain long-lived li-ion batteries. *Electrochem. Soc. Interface* **25**, 75–78 (2016).
19. Severson, K. A. *et al.* Data-driven prediction of battery cycle life before capacity degradation. *Nat. Energy* **4**, 383–391 (2019).
20. Attia, P. M. *et al.* Closed-loop optimization of fast-charging protocols for batteries with machine

- learning. *Nature* **578**, 397–402 (2020).
21. Aykol, M., Herring, P. & Anapolsky, A. Machine learning for continuous innovation in battery technologies. *Nat. Rev. Mater.* **5**, 725–727 (2020).
22. Konz, Z. M., McShane, E. J. & McCloskey, B. D. Detecting the onset of lithium plating and monitoring fast charging performance with voltage relaxation. *ACS Energy Lett.* **5**, 1750–1757 (2020).
23. Adam, A., Knobbe, E., Wandt, J. & Kwade, A. Application of the differential charging voltage analysis to determine the onset of lithium-plating during fast charging of lithium-ion cells. *J. Power Sources* **495**, 229794 (2021).
24. Colclasure, A. M. *et al.* Electrode scale and electrolyte transport effects on extreme fast charging of lithium-ion cells. *Electrochim. Acta* **337**, 135854 (2020).
25. Finegan, D. P. *et al.* Spatial dynamics of lithiation and lithium plating during high-rate operation of graphite electrodes. *Energy Environ. Sci.* **13**, 2570–2584 (2020).
26. Robertson, D. C. *et al.* Effect of Anode Porosity and Temperature on the Performance and Lithium Plating During Fast-Charging of Lithium-Ion Cells. *Energy Technol.* **9**, 1–14 (2021).
27. Chen, Y. *et al.* Operando video microscopy of Li plating and re-intercalation on graphite anodes during fast charging. *J. Mater. Chem. A* **9**, 23522–23536 (2021).
28. Dees, D. W. *et al.* Apparent Increasing Lithium Diffusion Coefficient with Applied Current in Graphite. *J. Electrochem. Soc.* **167**, 120528 (2020).
29. Uhlmann, C., Illig, J., Ender, M., Schuster, R. & Ivers-Tiffée, E. In situ detection of lithium metal plating on graphite in experimental cells. *J. Power Sources* **279**, 428–438 (2015).
30. Gao, T. *et al.* Interplay of Lithium Intercalation and Plating on a Single Graphite Particle. *Joule* **5**, 393–414 (2021).
31. Adam, A. *et al.* Development of an innovative workflow to optimize the fast-charge capability of lithium-ion battery cells. *J. Power Sources* **512**, 230469 (2021).
32. Gunnarsdóttir, A. B., Amanchukwu, C. V., Menkin, S. & Grey, C. P. Noninvasive in Situ NMR Study of ‘dead Lithium’ Formation and Lithium Corrosion in Full-Cell Lithium Metal Batteries. *J. Am. Chem. Soc.* **142**, 20814–20827 (2020).
33. Wandt, J., Jakes, P., Granwehr, J., Eichel, R. A. & Gasteiger, H. A. Quantitative and time-resolved detection of lithium plating on graphite anodes in lithium ion batteries. *Mater. Today* **21**, 231–240 (2018).
34. Tanim, T. R., Dufek, E. J., Dickerson, C. C. & Wood, S. M. Electrochemical Quantification of Lithium Plating: Challenges and Considerations. *J. Electrochem. Soc.* **166**, A2689–A2696 (2019).
35. Martin, C., Genovese, M., Louli, A. J., Weber, R. & Dahn, J. R. Cycling Lithium Metal on Graphite to Form Hybrid Lithium-Ion/Lithium Metal Cells. *Joule* **4**, 1296–1310 (2020).
36. Cai, W. *et al.* The Boundary of Lithium Plating in Graphite Electrode for Safe Lithium-Ion Batteries. *Angew. Chemie - Int. Ed.* **60**, 13007–13012 (2021).
37. Mei, W., Jiang, L., Liang, C., Sun, J. & Wang, Q. Understanding of Li-plating on graphite electrode: detection, quantification and mechanism revelation. *Energy Storage Mater.* **41**, 209–221 (2021).
38. Brown, D. E., McShane, E. J., Konz, Z. M., Knudsen, K. B. & McCloskey, B. D. Detecting onset of lithium plating during fast charging of Li-ion batteries using operando electrochemical impedance spectroscopy. *Cell Reports Phys. Sci.* **2**, 100589 (2021).
39. Ho, A. S. *et al.* 3D Detection of Lithiation and Lithium Plating in Graphite Anodes during Fast Charging. *ACS Nano* **15**, 10480–10487 (2021).
40. Duangdangchote, S. *et al.* Effect of fluoroethylene carbonate on the transport property of electrolytes towards Ni-rich Li-ion batteries with high safety. *Chem. Commun.* **57**, 6732–6735 (2021).
41. Yan, S. *et al.* Regulating the growth of lithium dendrite by coating an ultra-thin layer of gold on

- separator for improving the fast-charging ability of graphite anode. *J. Energy Chem.* **67**, 467–473 (2022).
42. Shin, H., Park, J., Sastry, A. M. & Lu, W. Effects of Fluoroethylene Carbonate (FEC) on Anode and Cathode Interfaces at Elevated Temperatures. *J. Electrochem. Soc.* **162**, A1683–A1692 (2015).
 43. Kazyak, E., Chen, K. H., Chen, Y., Cho, T. H. & Dasgupta, N. P. Enabling 4C Fast Charging of Lithium-Ion Batteries by Coating Graphite with a Solid-State Electrolyte. *Adv. Energy Mater.* **12**, (2022).
 44. Paul, P. P. *et al.* Quantification of heterogeneous, irreversible lithium plating in extreme fast charging of lithium-ion batteries. *Energy Environ. Sci.* **14**, 4979–4988 (2021).
 45. Christensen, J. & Newman, J. Cyclable Lithium and Capacity Loss in Li-Ion Cells. *J. Electrochem. Soc.* **152**, A818–A829 (2005).
 46. Gong, C. *et al.* Revealing the Role of Fluoride-Rich Battery Electrode Interphases by Operando Transmission Electron Microscopy. *Adv. Energy Mater.* **11**, 2003118 (2021).
 47. Logan, E. R., Tonita, E. M., Gering, K. L. & Dahn, J. R. A Critical Evaluation of the Advanced Electrolyte Model. *J. Electrochem. Soc.* **165**, A3350–A3359 (2018).
 48. Usseglio-Viretta, F. L. E. *et al.* Resolving the Discrepancy in Tortuosity Factor Estimation for Li-Ion Battery Electrodes through Micro-Macro Modeling and Experiment. *J. Electrochem. Soc.* **165**, A3403–A3426 (2018).
 49. Hindmarsh, A. C. *et al.* SUNDIALS: Suite of nonlinear and differential/algebraic equation solvers. *ACM Trans. Math. Softw.* **31**, 363–396 (2005).
 50. Bloom, I. *et al.* Differential voltage analyses of high-power, lithium-ion cells 1. Technique and application. *J. Power Sources* **139**, 295–303 (2005).

Supplementary Files

This is a list of supplementary files associated with this preprint. Click to download.

- [FINALv5SIForSubmission.pdf](#)